The 2010 IEEE/RSJ International Conference on
Intelligent Robots and Systems
October 18-22, 2010, Taipei, Taiwan

Image-Guided Robot-Assisted Microscope Objective Lens Positioning: Application in Patch Clamping

Mahdi Azizian, *Student Member, IEEE,* Rajni Patel, *Fellow, IEEE,* Cezar Gavrilovici and Michael Poulter

***Abstract*— There are applications where different objective lenses have to be used for microscope imaging. Rotary nosepieces cannot be used when larger objectives are required and when there is a physical space limitation. It is also very difficult and time consuming to change the objective lens manually and locate and focus on the same spot again; This may prevent any attempt for automating an image-guided robot-assisted procedure using the microscope images with different objective lenses. A linear lens changing mechanism has been developed which makes it possible to slide the objectives under a microscope. Image processing algorithms have been used to determine the optimal position of the lenses with respect to the source of light, compensate for changes in the focal length in case of non-parfocal objectives and to locate and focus on the exact same spot, regardless of the objective change. A 3-DOF micromanipulator has been used to move the microscope with respect to the substrate. As one of the most challenging applications, this can facilitate objective lens change in computer-assisted patch clamping with multiple electrodes.**

I. Introduction

Rotary objective nosepieces are usually used for changing objective lenses on a microscope; However, in some applications, it is not possible to use such an approach due to the larger size of objectives and physical space limitations. One of the applications where objective lens change becomes necessary is patch clamping which is an electrophysiological technique that permits the measurement of ion channel activity in many different kinds of cells [1]. To do multiple recordings, there is a need for multiple micromanipulators operating in a very limited space; Hence it is ideal to have a linear nosepiece to change the objective lenses. Doing this automatically, requires either an extremely accurate and pre-calibrated motorized system (which can be very expensive and also not useful for different objectives) or a high-resolution motorized system with online calibration and feedback control.

M. Azizian and R.V. Patel are with the Department of Electrical and Computer Engineering, University of Western Ontario and Canadian Surgical Technologies & Advanced Robotics (CSTAR), London, Ontario, Canada, e-mail: mazizian@uwo.ca, rvpatel@uwo.ca.

R.V. Patel is also with the Department of Surgery, University of Western Ontario, London, Ontario, Canada.

C. Gavrilovici and M. Poulter are with the Department of Physiology and Pharmacology, University of Western Ontario and Molecular Brain Research Group, Robarts Research Institute, London, Ontario, Canada, e-mail: cgavrilo@uwo.ca, mpoulter@robarts.ca.

This work was supported by an operating grant from the Canadian Institutes of Health Research (M.O. Poulter). The work of M. Azizian and R.V. Patel was partly supported by funds from the Natural Sciences and Engineering Research Council (NSERC) of Canada under grant RGPIN-1345 (R.V. Patel). Financial support for M. Azizian was also provided by an NSERC Alexander Graham Bell Canada Graduate Scholarship. C. Gavrilovici was supported by an Ontario Graduate Student Scholarship.

We have designed a 1-DOF high resolution prismatic manipulator which is capable of moving objective lenses with a high resolution along with a commercial 3-DOF micromanipulator (MP-285, Sutter Instruments) which is used to move the microscope with respect to the substrate. Image processing techniques can be used to achieve accurate position control [2]. We have developed image processing techniques for (a) finding the optimal position of each objective along the prismatic lens changing manipulator to align the objective with the source of light, (b) estimation of the focal length difference for non-parfocal objectives, (c) estimation of the planar shift of the images in the focal plane, (d) detecting the moment where a water immersion objective touches water surface and (e) automatic focusing on different objects [3]. The prismatic actuator and the 3-DOF micromanipulator provide robotic tools to compensate for errors detected by the image processing algorithms. The ultimate goal is to focus on the same spot when the lens is changed; The developed method should be accurate and repeatable regardless of (a) non-parfocal objectives, (b) image distortion and variable focal lengths (due to different water levels), (c) presence of noise in captured images, (d) illumination changes, and (d) limited accuracy of the micromanipulators and other imperfections existing in the hardware and optics.

In this paper, we have described the design of a prismatic lens changing manipulator (sliding nosepiece) along with the image processing algorithms developed for calibrating this sliding nosepiece. This is part of a computer-assisted patch clamping approach described in [4] which has capabilities such as master-slave control of micromanipulators, collision avoidance among micropipettes and visual servoing and position control of the micropipettes. This paper describes one major step towards using image-guided robot-assisted techniques in applications such as patch clamping where more than one objective lens is used and registration of the micromanipulator coordinates depends highly on whether the objective lens can be automatically changed.

In Section II the experimental setup is described. Optimal positioning of each objective lens with respect to the light source is described in Section III, water surface touch detection algorithm is described in Section IV while Section V provides more details on estimation of the focal length difference. Section VI discusses the estimation of the planar offset between the center of images for different objectives. The overall automatic objective lens change procedure is described in Section VII and the experiments are described in Section VIII. Section IX concludes the paper with some suggestions for future work.

II. Experimental Setup

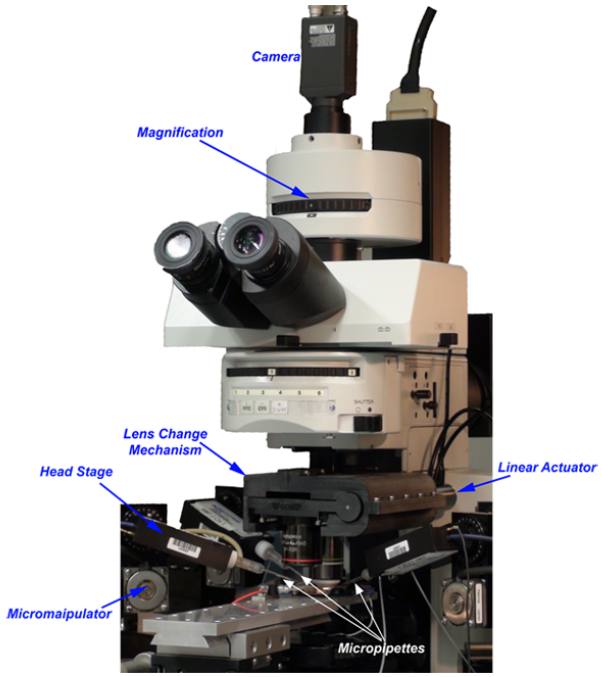

Fig. 1. Experimental setup illustrating the microscope, micromanipulators and the prismatic manipulator developed for lens changing.

The experimental setup is shown in Figure 1. In this paper we are focusing on the custom-designed prismatic lens changing mechanism. The 1-DOF prismatic actuator has been developed to change the objective lenses. A CAD model is illustrated in Figure 2 and the actual system can be seen in Figure 1 installed on a microscope. The linear actuator is T-LA60A-S, Zaber Technologies with $60mm$ range of motion (we only use $50mm$), $1\mu m$ repeatability and $4mm/sec$ maximum linear speed. The linear actuator has $0.1\mu m$ as its default resolution (what we use) and $0.05\mu m$ as the finest resolution; It also shows less than $4\mu m$ backlash. Two extension springs ($77.5N/m$) have been used for the return mechanism. The mechanism can be simply adapted for different objective lenses by choosing a different objective holder plate.

The mechanism shows the same repeatability as the linear actuator so long as the motion is not blocked. The low friction linear bearings guarantee a smooth motion without any blocking.

III. Optimal Objective Lens Positioning

To obtain better image quality, the objective lens should be aligned with the light source. If it is not completely aligned, more illumination will be required and the microscope image quality will be degraded. To achieve this goal, the user is asked to close the diaphragm and then slightly open it to create a point light source. Then the prismatic actuator moves the objective back and forth to find the location with maximum illumination for the specified objective lens. To save time, the objective is located on its pre-known

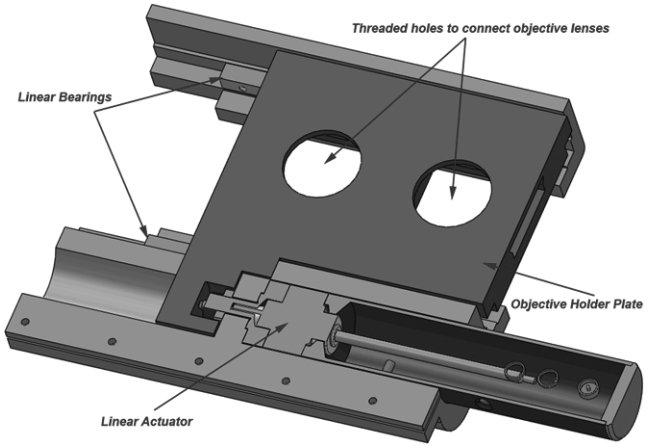

Fig. 2. A CAD model of the prismatic lens changing manipulator. (The returning springs are not visible in this picture, but can be seen in Figure 1)

location (known from the previous calibration). To calibrate the system for the first time, the user is asked to specify an initial position. This procedure is performed for all objective lenses and the optimal location for each lens is saved. The optimization criterion is simply:

$$J_1(d) = \sum_{i=1}^{M}\sum_{j=1}^{N} e^{-\frac{1}{\sigma}\sqrt{(i-\frac{M}{2})^2+(j-\frac{N}{2})^2}} I(i,j) \qquad (1)$$

where d is the objective location measured in μm and M, N are the width and height of the image in pixels respectively and $\sigma = \frac{1}{2}\frac{\sqrt{M^2+N^2}}{\log(I_{max})}$ and $[0, I_{max}]$ is the dynamic range of image pixel intensities, where $I_{max} = 255$ as we are using 8-bit image depth. The exponential term is used to weight the points based on their distance from the center of the image because the goal is to locate the position where a point-wise light source is seen as a circle centered in the images. The whole range of motion for the prismatic lens actuator is $50mm$ and each lens is moved $\pm 2mm$ around its initial position to find the optimal location. Plots of J_1 vs d are shown in Figure 3 for each of the lenses.

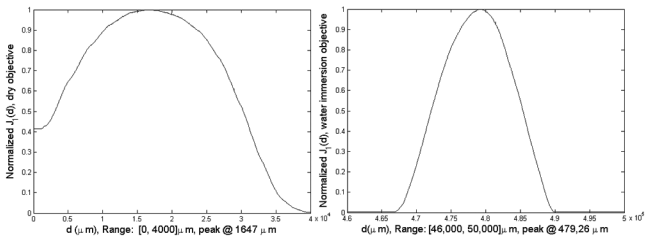

Fig. 3. $J_1(d)$ vs. $d(\mu m)$ Illumination curves for optimal positioning of a $4\times$ dry objective (left) and a $20\times$ water immersion objective (right)

The experiment has been repeated 20 times for each objective. The optimal point for the $4\times$ lens was measured to be at $1647 \pm 44.661(\mu m)$ and for the $20\times$ lens, it was at $47926 \pm 25.267(\mu m)$. The error in locating the optimal lens location is mainly due to the non-ideal light source (it is not an ideal point source) and the interference of illumination and noise from other sources.

IV. Detection of Water Surface Touch

A water immersion lens should touch the water surface before it can be used. The objective lens is moved down slowly till it touches the water surface and then it goes back to its original height while pulling the water via its surface tension. The three steps of this procedure are shown in Figure 4.

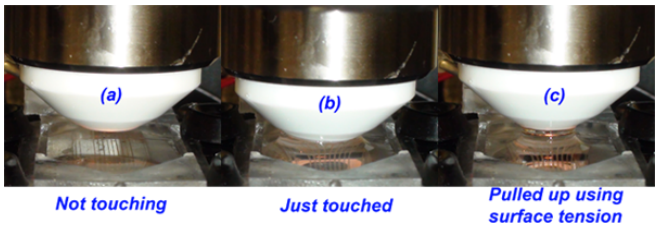

Fig. 4. Water Surface Touch: (a) Before touching the water surface, (b) while touching, and (c) back up with stretched water surface.

Water surface contact is detected by a sudden change in illumination of the image. The temporal gradient of the images is calculated at each time step and when it is higher than a pre-defined threshold, the software stops the objective and asks the user to verify if the objective has actually made contact with the water surface. Then the objective is moved up to its original position or it keeps moving down if the goal has not been achieved. The user can stop the motion in case the water surface has been touched if the software fails to recognize it. We calculate a normalized integrated temporal gradient of the images as $\mathcal{F}_z(\mathcal{I})$.

$$\mathcal{F}_z(\mathcal{I}) = \frac{||\nabla_t \mathcal{I}||}{||\mathcal{I}||} = \frac{\sum_{i=1}^{M}\sum_{j=1}^{N}|\mathcal{I}_k(i,j) - \mathcal{I}_{k-1}(i,j)|}{\sum_{i=1}^{M}\sum_{j=1}^{N}\mathcal{I}_{k-1}(i,j)} \tag{2}$$

The threshold is determined empirically by the user. For our experiments, a threshold of $\tau = 0.05(5\%)$ works fine. It should be mentioned that if the initial illumination is too much, i.e. a very bright image is captured out of water, this method may not work properly because the image is already saturated; Also if the initial illumination is too low, there will not be enough light to detect the change. The method may also fail if the user suddenly changes the light intensity when the algorithm is running. $\mathcal{F}_z(\mathcal{I})$ and also the normalized average image intensities ($\bar{\mathcal{I}}(k) = \frac{\sum_{i=1}^{M}\sum_{j=1}^{N}\mathcal{I}_k(i,j)}{MNI_{max}}$) have been evaluated in four different cases with the initial $\bar{\mathcal{I}}$ changing roughly from 30% to 70%. The results are represented in Figure 5.

The method is robust to different illumination levels. Peaks are easily detectable in $\mathcal{F}_z(\mathcal{I})$ at the moment when the objective touches the water surface as shown in Figure 5.

V. Estimation of the Difference in Focal Lengths

We have used a $4\times$ dry lens and a $20\times$ water immersion lens which are not parfocal; This means that even if the objective position is adjusted accurately, the same scene will not be visible under both objectives. We have used

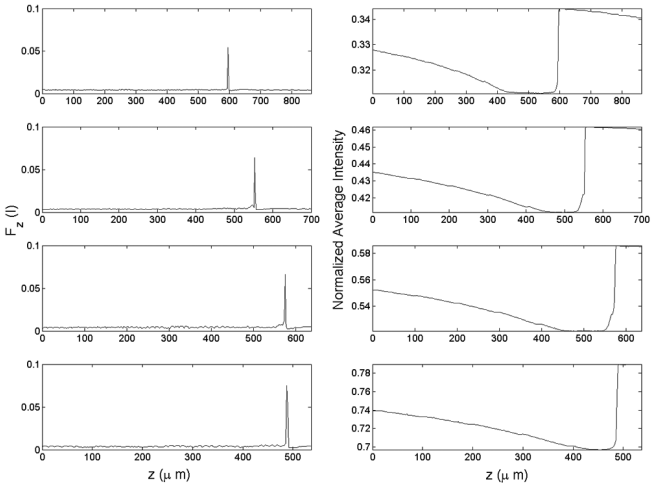

Fig. 5. The graphs on the left show $\mathcal{F}_z(\mathcal{I})$ vs. z and the graphs on the right show $\bar{\mathcal{I}}$ vs. z for four experiments with different light intensity.

the autofocusing algorithm [3] to estimate the difference in focal length of the two objectives. However, the focal length change is not a very accurate measure due to the variable water level. The dry lens shows variable focal lengths due to different refractive index for water and air. The water immersion lens implies distortion in the images based on the way it is connected to the water surface. The goal is to find an estimation of the focal length change. Once the objective lens is changed and the target spot is close to focus, the autofocusing algorithm will move the objective to bring the desired object into focus.

We have chosen a mesh as a target as shown in Figure 7 and we focus on it using the dry objective. Then we change to the water immersion objective and we autofocus on the mesh (at the same spot). We repeat this procedure for three different water levels. The vertical position of the microscope is recorded in each case and the results are shown in Table I.

Water Level	$z_{4\times}(\mu m)$	$z_{20\times}(\mu m)$	$\delta f(\mu m) = z_{4\times} - z_{20\times}$
Low	-375.8	-3423.5	3047.7
Medium	386.9	-3287.7	3674.6
High	620.2	-3261.4	3881.6

TABLE I
Estimation of the focal length difference

We use the estimation of δf for low water levels because it is safer when we change from dry to water immersion objective. The objective can be moved down to autofocus afterwards; this prevents breaking of the micropipette tips.

VI. Estimation of the Planar Offset

Although we have adjusted the objective lenses on the optimal locations using the source of the light as a reference and we can compensate for the difference in focal lengths, the centers of the images acquired by each lens may have a planar shift due to imperfect structure of the objective lens actuator and other factors. As the water immersion lens has 5 times more magnification, the visible area will be 25 times

smaller and even a small planar shift may result in the target going out of the field of view; Due to this fact, we have used a registration algorithm to estimate this planar shift by capturing a bigger area by moving the objective lens around. The objective lens is then moved in a spiral pattern to capture a larger area by stitching the images together. The spiral motion pattern along with the stitched images is illustrated in Figure 6.

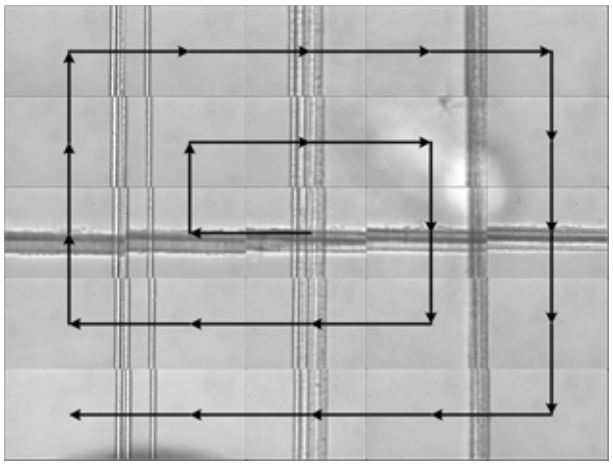

Fig. 6. Spiral pattern for capturing and stitching images. The stitching is not perfect due to lens distortion and imperfect calibrations (causing errors in pixel size).

The spiral motion is performed based on the pixel size estimation calculated during system calibration [3], [4]. The pixel size is estimated to be $0.6724\mu m$ for the water immersion lens. The motion is performed based on the real image size $430.336 \times 322.752\mu m$ (640×480 pixels). 25 images are captured and stitched together to create a bigger size image. The acquired image has a higher number of pixels but smaller pixel-size compared to the image captured by the $4\times$ dry lens. We downsample the image by a factor of 5 after smoothing it by a Gaussian filter [5]. Now we have two images with the same size and same pixel size that we can register to find the planar shift which is the distance $(\delta x,\ \delta y)$ of the centers of the images in their focal planes. We assume that the focal planes are parallel which is a valid assumption so long as lens distortion is not involved. To estimate these parameters, we need to register images obtained by the two objectives. This can be used for calibrating the system to perform the lens change automatically.

When the objective is changed from a dry lens to a water-immersion lens, the properties of the image change a lot as shown in Figure 7; a list of these differences is following:

- *Scale*: the actual pixel size is changed by a factor of 5 due to the higher magnification of the water-immersion lens ($20\times$ compared to $4\times$). However, the size of the image does not change which will cause a smaller region to be visible in the image with the $20\times$ lens, but it will show more details due to the smaller pixel size.
- *Distortion*: while the dry objective has a negligible distortion, the water immersion objective causes a non-linear and variable distortion due to contact with the water surface.
- *Illumination*: with a constant light intensity and unchanged shutter, there is a huge change in the visible illumination of the images captured by different lenses. Although the user is asked to adjust the illumination, it usually will not be the same for both cases.
- *Focus*: A part of the scene may be out of focus for each of the lenses. This is due to the non-flat surface of the object under the microscope. The object is usually non-flat and will not be in the same focal plane.
- *Image Stitching Errors*: There will be some error caused by stitching of the images captured by the water immersion objective.

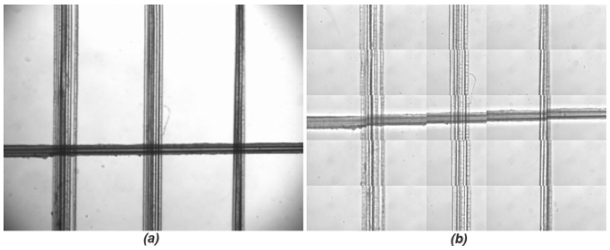

Fig. 7. Same scene viewed (a) by the $4\times$ dry objective ($\mathcal{I}_{4\times}$) and (b) by the $20\times$ water immersion objective by moving the objective and stiching captured images ($\mathcal{I}^a_{20\times}$).

The goal is to register the images grabbed by a water immersion lens to the image(s) grabbed by the dry objective. A registration method could be used for detecting translation between $\mathcal{I}_{4\times}$ and $\mathcal{I}^a_{20\times}$. Phase correlation is an area-based registration method using the shift property of the Fourier transform [6] and it can be used to find translation, rotation and scaling between two images or an image and a template with a pixel or even sub-pixel accuracy [7], [8]. It has gained a lot of popularity in global or local image registration due to its accuracy and robustness to uniform variations of illumination and noise in images [8]. The method is described in more detail in [3] for detection and tracking of micropipette tips under the water immersion objective. We have used the same method, the only difference is that before applying the phase correlation based registration to the images, we adjust the intensities of each image to increase the contrast and to partially compensate for the variable illumination of the images. The result of the phase correlation technique applied to the images in Figure 7 is shown in Figure 8.

Once the objective lens positioning is done, the microscope calibration data is updated for the water immersion lens. The user will be able to bring the slice into focus and then click and locate the micropipettes on top of the slice and start approaching the cells using the haptic device and the master/slave control as described in [4].

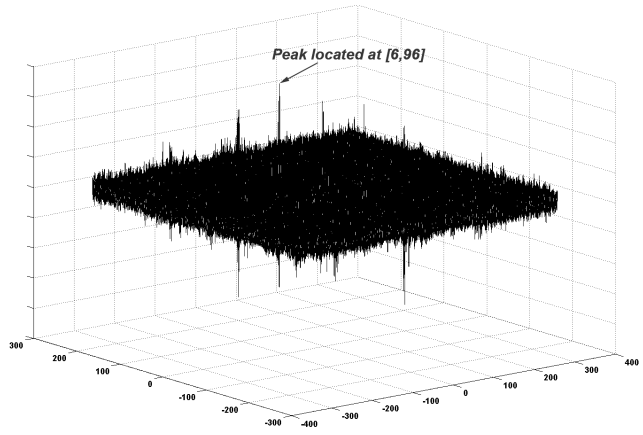

Fig. 8. Phase correlation technique applied to images in Figure 7 detects a displacement of [6,96] pixels which makes sense considering the vertical displacement visible in the images. The resulting displacement will be $(\delta x, \delta y) = (20.172, 322.752)\mu m$.

VII. Automatic Objective Lens Change

When the $4\times$ dry objective lens is in use, the user locates the area of the tissue slice which contains cells that are to be studied. This is usually chosen close to the edges of the slice. A sample image is shown in Figure 9(b).

Fig. 9. (a) Prepared slice before being used, (b) Slice under the $4\times$ dry objective; (the actual width of the image is $2.151mm$).

Then the objective is moved up automatically and the micropipettes are brought in the field of view based on the calibration information. The objective and micropipettes are then moved down until they are on top of the slice. The user can move and adjust the relative location of the slice and micropipettes using the software. Then the software pulls out the micropipettes along their central axis automatically (this will guarantee that they will not collide with the substrate, the objective or other micropipettes). The objective lens is then changed automatically following these steps:

1) The objectives are moved up to make sure the objective lenses will not hit the substrate when shifting.
2) The prismatic manipulator brings the water immersion objective forward to its optimal location as determined in Section III.
3) The microscope is moved in plane to compensate for the planar shift as described in Section VI.
4) The microscope is moved down to its original position plus δf to compensate for the focal length difference.
5) If it is not touching the water surface (which happens in most cases), the objective is moved down till it touches water surface (as described in Section IV) and then returns to the starting position pulling up the water surface as shown in Figure 4.

Then the micropipettes are brought in on the same path as they were pulled out. There is still a possibility that the micropipette tips are not visible due to the variable focal length difference as described in Section V. The autofocusing algorithm is then used to bring the micropipettes into focus by moving the objective down.

VIII. Experiments

Details of using the developed software to perform patch clamping has been described in [4]. The automatic lens change is described in the previous section and the details of preparing brain slices, patch clamp electrophysiology and 3D image reconstruction are described in this section.

A. Brain slicing procedures and tissue maintenance

Coronal rat brain slices ($350\mu m$; 1.5 to $-0.3mm$ relative to bregma) were performed according to published methodology [9]. Slicing, incubation, and storage are all performed in the choline solution. The Ringer's solution used during electrical recordings is similar to the choline solution except that pyruvate and ascorbate are removed, equimolar $NaCl$ replaced the choline Cl, and $MgCl_2$ is used at a $2mM$ concentration. All solutions are maintained at pH 7.4 and bubbled with $5\% - CO_2$ / $95\% - O_2$ (carbogen).

B. Electrophysiology

Patch electrodes were pulled from borosilicate glass capillaries and filled with K-gluconate solution (300 mOsm, pH 7.3-7.4). Voltage-gated currents and excitability of cells in layers II and III of piriform cortex were monitored by means of voltage-clamp and current-clamp protocols (PulseFit v 8.0; Heka, Germany). The results are shown in Figures 10.

C. Immunohistochemistry and image acquisition

In order to reconstruct the morphology and understand where the recordings are made, biocytin was included in patch microelectrode solution. After the completion of a recording, the slice was removed from the microscope chamber and fixed in 4% paraformaldehyde (PFA) for at least 24 h. After rinsing [10] the slices were incubated in streptavidin-conjugated Alexa Fluor-594 ($5\mu g/ml$; Molecular Probes) and mounted onto Fisher SuperFrost slides and mounted with glass coverslips in Prolong Gold Antifade mounting medium (Molecular Probes, Eugene, OR). Confocal images were taken on an Olympus IX 60 inverted microscope outfitted with a Perkin Elmer Spinning Disk Confocal attachment with a 20X (N.A. = 0.50) objective. The microscope was equipped with a Hamatsu Orca ER CCD camera (1300×1030 pixels), and images were acquired in Volocity software (Improvision, Lexington, MA). Each image represents a stack of 40–50 images $0.2\mu m$ apart in the z-plane. For morphological reconstruction of the dendritic arborization of patched neurons, the stacks of confocal images were deconvolved with AutoQuant

software (AutoQuant Imaging, Burnbury, Ontario, Canada) and then processed with Imaris Filament Tracer module in *surpass mode* (Bitplane, Zurich, Switzerland). To mark the cell bodies, an *Isosurface* was then created. This process creates a cell body from the stack of images that is then merged with the dendritic morphology (Figure 12).

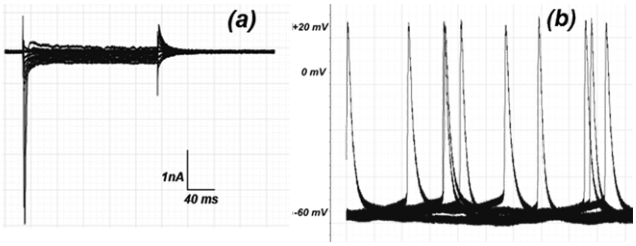

Fig. 10. (a) Voltage clamp recording of a patch clamped interneuron (downward traces showing sodium current flow) and (b) Neuronal firing pattern of a patch clamped interneuron (upward traces indicate action potentials) - Cell A as shown in Figure 12 in layer III of rat piriform cortex.

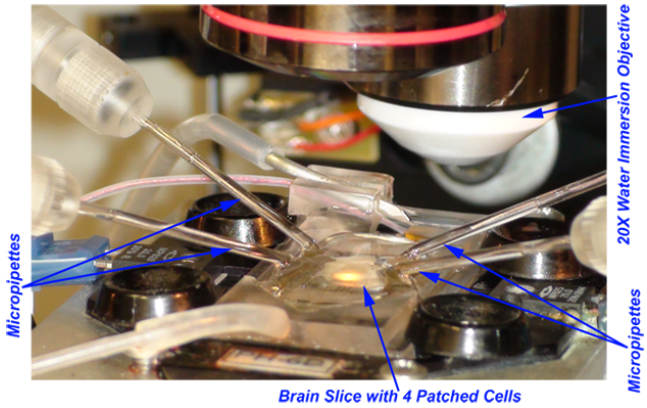

Fig. 11. Brain slice with four patched cells, the objective lens is changed to provide better visibility in the picture.

IX. Conclusion and Future Work

We have developed a computer-assisted patch clamping technique as described in [4]. In this paper, we reported the development of 1-DOF prismatic actuator for automatic objective lens change where positioning errors and offsets are being estimated using image processing algorithms. This is a critical step towards automating procedures such as patch clamping and other types of multi-objective microscope image-guided micromanipulation. Using image processing techniques for system calibration and positioning error compensation has the benefit of using a not expensive actuator instead of a very expensive highly accurate pre-calibrated system. It also makes it very flexible to be used with different systems. Results of an actual four electrode patch clamping using this system have also been reported which shows effectiveness of the developed method.

Our ongoing work is looking into methods for estimating the variable focal length caused by varying water levels and compensating for it. We are also looking into methods for evaluating and compensating for the lens distortion and stitching methods to increase the efficiency of the registration technique we have used.

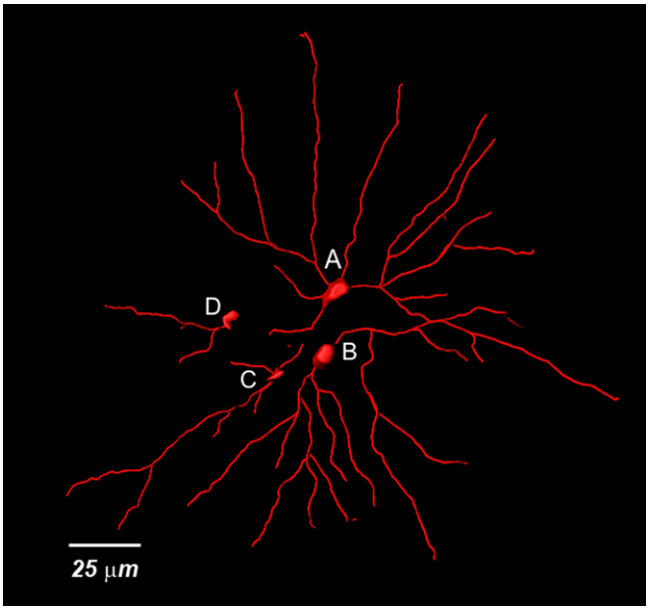

Fig. 12. Morphological reconstruction of four interneurons in layer III of piriform cortex as shown in Figure 11. Partial cell body and dendritic arborization reconstruction for cell C and D indicate a lighter biocytin staining of these neurons.

References

[1] A. Molleman, *Patch Clamping: An Introductory Guide to Patch Clamp Electrophysiology*, 1st ed. Wiley, 2003.

[2] Q. Xu, Y. Li, and N. Xi, "Design, fabrication, and visual servo control of an xy parallel micromanipulator with piezo-actuation," *IEEE Transactions on Automation Science and Engineering*, vol. 6, no. 4, pp. 710–719, 2009.

[3] M. Azizian, R. Patel, C. Gavrilovici, and M. Poulter, "Image processing techniques in computer-assisted patch clamping," in *Imaging, Manipulation, and Analysis of Biomolecules, Cells, and Tissues VIII*, vol. 7568. SPIE, 2010, pp. 75 681E1–75 681E12.

[4] M. Azizian, R. V. Patel, C. Gavrilovici, and M. O. Poulter, "Computer-assisted patch clamping," in *Proceedings of the IEEE International Conference on Robotics and Automation (ICRA)*, 2010.

[5] D. G. Lowe, "Distinctive image features from scale-invariant keypoints," *International Journal of Computer Vision*, vol. 60, no. 2, pp. 91–110, 2004.

[6] B. Zitova and J. Flusser, "Image registration methods: a survey," *Image and Vision Computing*, vol. 21, no. 11, pp. 977–1000, 2003.

[7] B. Reddy and B. Chatterji, "An FFT-based technique for translation, rotation, and scale-invariant image registration," *IEEE Transactions on Image Processing*, vol. 5, no. 8, pp. 1266–1271, 1996.

[8] H. Foroosh, J. Zerubia, and M. Berthod, "Extension of phase correlation to subpixel registration," *IEEE Transactions on Image Processing*, vol. 11, no. 3, pp. 188–200, 2002.

[9] C. Gavrilovici, S. D'Alfonso, M. Dann, and M. O. Poulter, "Kindling-induced alterations in gabaa receptor mediated inhibition and neurosteroid activity in the piriform cortex of rat," *European Journal of Neuroscience*, vol. 24, no. 5, pp. 1373–1384, 2006.

[10] C. Gavrilovici, S. D'Alfonso, and M. O. Poulter, "Diverse interneuron populations have highly specific interconnectivity in the rat piriform cortex," *Journal of Comparative Neurology*, vol. 518, no. 9, pp. 1570–1588, 2009.